

C. Jacobsen, R. Medenwaldt, and S. Williams

“A perspective on biological x-ray and electron microscopy”

In J. Thieme, G. Schmahl, E. Umbach, and D. Rudolph, eds., *X-ray Microscopy and Spectromicroscopy* (Springer-Verlag, Berlin, 1998), pp. 93-102

A Perspective on Biological X-Ray and Electron Microscopy

Chris Jacobsen¹, Robin Medenwaldt², Shawn Williams³

¹ Department of Physics, SUNY Stony Brook, Stony Brook NY 11794-3800, USA

² Institute for Storage Ring Facilities, University of Aarhus, Ny Munkegaade, DK-8000 Aarhus C, Denmark

³ Boyer Center for Molecular Medicine, Yale University, New Haven CT 06510, USA

Abstract. We consider image contrast for electron microscopy of thick hydrated biological specimens, allowing for the use of phase contrast and energy filtering. This allows us to gain perspective on the relative roles of electron and soft X-ray microscopes. Radiation dose is found to depend strongly on ice thickness, with electrons offering lower dose if the ice thickness is less than about 500 nm, and x rays offering lower dose for thicker ice layers.

1 Introduction

Native biological structures are wet structures. The preferred tool for studying such structures often is visible light microscopy, provided the resolution is sufficient for the study at hand (near-field techniques [1] and deconvolution methods [2] can be used to study < 100 nm structures in favorable circumstances). However, both X-ray and electron microscopy offer higher spatial resolution as well as capabilities for elemental and chemical state mapping. These shorter wavelength probes come at a cost in loss of convenience and, more fundamentally, a cost in terms of damage caused by the ionizing radiation used if electrons or x rays are chosen. For that reason, cryofixation is often used for electron microscopy of hydrated structures, and it is beginning to find application in X-ray microscopy as well.

Which ionizing probe is better for high resolution studies: electrons or X-rays? On the one hand, arguments based on a high ratio of elastic to inelastic scattering and the low (~ 40 eV as will be discussed) energy transfer of inelastic events point to electron microscopy as offering intrinsic advantages for atomic resolution microscopy [3, 4]. On the other hand, calculations by Sayre *et al.* [5] and others (see e.g., [6, 7]) suggest that X-ray probes offer lower radiation dose. While Monte Carlo models of image contrast for frozen hydrated specimens in electron microscopy have been considered by Schröder [8], we consider here an analytical model. The present work differs from that of Sayre *et al.* in that it assumes the availability of phase contrast in both electron and X-ray microscopy. Radiation dose is found to depend strongly on ice thickness, with electrons offering lower dose if the ice thickness is less than about 500 nm, and x rays offering lower dose for thicker ice layers.

2 Electron Interactions

2.1 Cross Sections

When passing through a solid, electrons undergo elastic scattering with a wide range of angular deflections, and inelastic scattering. The cross sections for these interactions are well approximated by simple expressions as is described by Langmore and Smith [9], who extend earlier work by Langmore *et al.* [10] and Wall *et al.* [11]. For our purposes, we will speak of three cross sections: σ_{el} for elastic scattering, σ_{inel} for inelastic scattering, and η for the fraction of elastic scattering events in which the scattered electron does *not* pass through the objective aperture in the microscope. The main case where these expressions are inaccurate is for inelastic scattering of hydrogen; we follow Langmore and Smith [9] in using their empirically determined value of $\sigma_{\text{inel}} = 8.8 \text{ pm}^2$ at 80 keV with scaling to other voltages in our calculations. Finally, the angular distribution of inelastically scattered electrons is small enough to assume that all such electrons remain within the angular extent of the objective aperture.

These atomic scattering results can be extended to molecules and larger structures if one assumes the specimen to be amorphous over length scales smaller than the one of interest, such as is typically the case for dose-limited electron microscopy of thicker specimens. The net cross section σ_m and objective aperture exclusion fraction η_m for a collection of atoms (such as a molecule viewed at moderate resolution, where diffraction peaks from bonds are ignored) can be found by summation of effects on its constituent atoms:

$$\sigma_m \eta_m = \sum_{n=1}^{n=N_m} [\sigma(n) \eta(n)], \quad (1)$$

where N_m is the number of atoms in the molecule. The probability for scattering is then

$$P = \sigma_m \eta_m \delta_m t_m, \quad (2)$$

where δ_m is the number density of molecules and t_m is the thickness of the molecular layer. We can then speak of a probability K per thickness for three interactions:

$$P_{\text{inel}} = K_{\text{inel}} t_m = \sigma_{\text{inel}} \delta_m t_m \quad (3)$$

$$P_{\text{el,in}} = K_{\text{el,in}} t_m = \sigma_{\text{el}} (1 - \eta_{\text{el}}) \delta_m t_m \quad (4)$$

$$P_{\text{el,out}} = K_{\text{el,out}} t_m = \sigma_{\text{el}} \eta_{\text{el}} \delta_m t_m \quad (5)$$

$$P_{\text{tot}} = K_{\text{tot}} t_m = (K_{\text{inel}} + K_{\text{el,in}} + K_{\text{el,out}}) t_m \quad (6)$$

where P_{inel} refers to inelastic scattering, and $P_{\text{el,in}}$ and $P_{\text{el,out}}$ refer to elastic scattering *into* and *out of* the objective aperture, respectively. (All of these probabilities P and probabilities per thickness K are expressed in the limit of weak scattering per atom). Alternatively, we can also consider the mean free path for various interactions $\lambda = 1/K$; mean free paths calculated for electrons in vitreous ice ($\rho = 0.92 \text{ g/cm}^3$) and for a “generic” protein ($\text{H}_{48.6}\text{C}_{32.9}\text{N}_{8.9}\text{O}_{8.9}\text{S}_{0.6}$,

$\rho = 1.35 \text{ g/cm}^3$ as per [12]) are shown in Fig. 1. It should be noted that the inelastic mean free path used here differs significantly from that assumed in some calculations [8, 13], but agrees well with several experimental observations [14, 15].

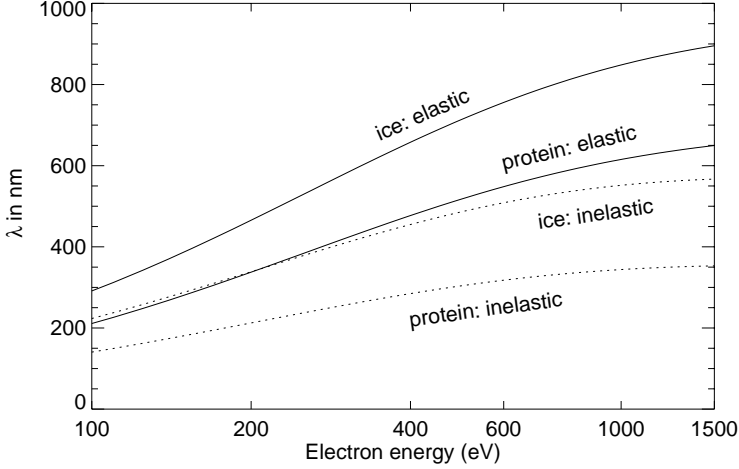


Fig. 1. Mean free paths λ calculated for electrons in vitreous ice and in amorphous protein.

2.2 Energy Transfer

Inelastically scattered electrons cause ionizing radiation damage to the specimen. We must therefore consider the energy ΔE transferred in inelastic scattering events. For biological specimens, we will assume that inelastic scattering in ice dominates, since organic materials will be hydrated and distributed within ice. For radiation dose calculations, we wish to know what is the typical energy deposition E for an inelastic scattering event. The low probability of high ΔE inelastic scattering events is partly offset by the large amount of energy they deposit. The typical energy deposition E can be calculated from the probability distribution $s_1(E)$ for electron energy loss as

$$\frac{\int_0^E s_1(E) E dE}{s_1 E_{\text{tot}}} = \frac{1}{2} \text{ where } s_1 E_{\text{tot}} \equiv \int_0^\infty s_1(E) E dE. \quad (7)$$

Using EELS spectra of vitreous ice provided by R. Leapman of the National Institutes of Health (see also [15]), we calculate $E = 46 \text{ eV}$ for ice, whereas

Isaacson [16] gives $E = 37.5$ eV for dehydrated nucleic acid bases. The linear energy transfer

$$\frac{dE/dx}{\rho} = \frac{E}{\lambda_{\text{inel}}\rho} \quad (8)$$

calculated from these inelastic scattering cross sections and mean energy transfers is about a factor of two lower than that given in the commonly-used calculation of Berger and Seltzer [17]; this discrepancy is likely due to an overestimate of plasmon mode losses in Berger and Seltzer's calculations [18]. Using $E = 37.5$ eV and $\lambda_{\text{inel}} = 139$ nm at 100 keV to give $(dE/dx)/\rho = 2.0$ MeV · cm²/g, one can estimate that an electron exposure of 1 e⁻/nm² corresponds to a dose of 3.2×10^4 Gray.

2.3 Electron Categories

Using expressions given below, we calculate the relative intensity of electrons in a variety of categories: I_{noscat} refers to electrons which have not been scattered at all; I_{1el} refers to electrons which have undergone only one elastic scattering and which remain within the objective aperture; I_{multel} refers to electrons which have undergone multiple elastic scatterings, no inelastic scatterings, and which remain within the objective aperture; I_{inel} refers to electrons which have undergone at least one inelastic scattering yet which remain within the objective aperture; and I_{out} refers to electrons which have been scattered outside the angular acceptance of the objective aperture. It can be shown that

$$I_{\text{noscat}} + I_{\text{1el}} + I_{\text{multel}} + I_{\text{out}} + I_{\text{inel}} = I_0, \quad (9)$$

so that we can consider all of the electrons to belong to one of these categories. While these expressions have limitations in describing some of the subtleties of plural scattering, they are useful as a first approximation. A plot of the fraction of electrons in each of these categories as a function of ice thickness is shown in Fig. 2.

3 Electron Microscopy Image Contrast and Dose

Image contrast of thin specimens in electron microscopy is well understood (see e.g., [19]). Amplitude contrast of specimens which are thick compared to a mean free path for elastic scattering (typically 100 nm) has been considered by several authors (see e.g., [5, 20]). However, the intrinsic contrast of native biological structures in vitreous ice tends to be rather low, so that in fact most work is done using defocus (to produce phase contrast) and energy filters which efficiently remove inelastically scattered electrons from the image plane of the microscope [21]. Schröder has made Monte Carlo calculations of a parameter related to image contrast of some specific model systems relevant to cryomicroscopy with energy filtering [8]. Our approach builds heavily upon the work of Sayre *et al.* [5] and Langmore and Smith [9].

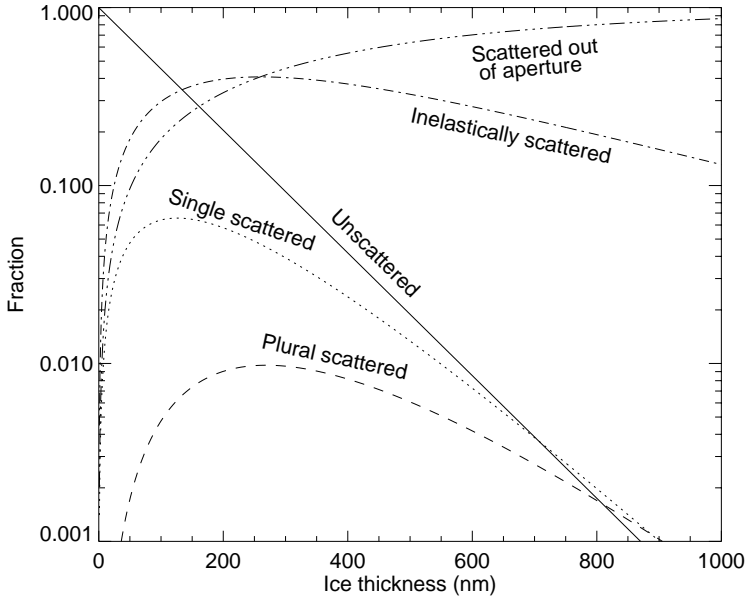


Fig. 2. Normalized intensity of 100 keV electrons in various categories as a function of thickness of vitreous ice. For phase contrast one desires interference between unscattered and single scattered electrons, but this signal declines steeply with increased ice thickness and furthermore the plural scattered signal rises to similar values. In thick ice layers it is exceedingly important to remove inelastically scattered electrons using an imaging energy filter, for otherwise these electrons contribute an out-of-focus haze due to the fact that they are not well focused by electron optics which have intrinsic chromatic aberrations.

The above calculations allowed us to categorize electrons after passage through a thickness t of an amorphous material. We now modify these calculations to consider passage through a thickness t_f of a feature embedded within a thickness $t_b = t - t_f$ of a “background” material matrix. We then calculate the signal difference between the feature-present I_f and the feature absent I_b case and divide it by the square root of the sum of the two signals to account for electron statistics [22], giving a contrast $\Theta = (I_f - I_b)/\sqrt{I_f + I_b}$. The number of electrons N required to see an object with a signal-to-noise ratio of 5:1 is then $N = 25/\Theta^2$. One can calculate Θ for a variety of imaging modes [5]; we restrict ourselves here to brightfield imaging with and without phase contrast, and with and without the use of energy filters. Using the expressions

$$I_{\text{noscat},b} = I_0 \exp[-K_{\text{tot},b}t] \quad (10)$$

$$I_{\text{1el},b} = K_{\text{el},\text{in},b} t I_{\text{noscat},b} \quad (11)$$

$$I_{\text{in,noinel},b} = I_0 \exp[-(K_{\text{inel},b} + K_{\text{el},\text{out},b})t] \quad (12)$$

$$I_{\text{multel},b} = I_{\text{in,noinel},b} - I_{\text{noscat},b} - I_{1\text{el},b} \quad (13)$$

$$I_{\text{in},b} = I_0 \exp[-K_{\text{el,out},b}t] \quad (14)$$

$$I_{\text{el,out},b} = I_0 - I_{\text{in},b} \quad (15)$$

$$I_{\text{inel},b} = I_{\text{in},b} - I_{\text{in,noinel},b} \quad (16)$$

(which were used to calculate Fig. 2) and

$$I_{\text{noscat},f} = I_0 \exp[-K_{\text{tot},b}t_b] \exp[-K_{\text{tot},f}t_f] \quad (17)$$

$$I_{1\text{el},f} = (K_{\text{el,in},b}t_b + K_{\text{el,in},f}t_f)I_{\text{noscat},f} \quad (18)$$

$$I_{1\text{el}/f,f} = K_{\text{el,in},f}t_f I_{\text{noscat},f} \quad (19)$$

$$I_{\text{in,noinel},f} = I_0 \exp[-(K_{\text{inel},b} + K_{\text{el,out},b})t_b] \exp[-(K_{\text{inel},f} + K_{\text{el,out},f})t_f] \quad (20)$$

$$I_{\text{multel},f} = I_{\text{in,noinel},f} - I_{\text{noscat},f} - I_{1\text{el},f} \quad (21)$$

$$I_{\text{in},f} = I_0 \exp[-K_{\text{el,out},b}t_b] \exp[-K_{\text{el,out},f}t_f] \quad (22)$$

$$I_{\text{el,out},f} = I_0 - I_{\text{in},f} \quad (23)$$

$$I_{\text{inel},f} = I_{\text{in},f} - I_{\text{in,noinel},f} \quad (24)$$

we obtain results for imaging without phase contrast and with and without energy filtering of

$$\Theta_B = \frac{|I_{\text{in,noinel},f} - I_{\text{in,noinel},b}|}{\sqrt{I_{\text{in},f} + I_{\text{in},b}}} \quad (25)$$

$$\Theta_{\text{BF}} = \frac{|I_{\text{in,noinel},f} - I_{\text{in,noinel},b}|}{\sqrt{I_{\text{in,noinel},f} + I_{\text{in,noinel},b}}} \quad (26)$$

respectively. In the case of phase contrast with the optimum defocus for a spatial frequency of interest, we find that the contrast is given by

$$\Theta_{B,\varphi} = \frac{|I_{\text{in,noinel},f} - I_{\text{in,noinel},b}| + 2\sqrt{I_{\text{noscat},f}I_{1\text{el}/f,f}}}{\sqrt{I_{\text{in},f} + I_{\text{in},b}}} \quad (27)$$

$$\Theta_{\text{BF},\varphi} = \frac{|I_{\text{in,noinel},f} - I_{\text{in,noinel},b}| + 2\sqrt{I_{\text{noscat},f}I_{1\text{el}/f,f}}}{\sqrt{I_{\text{in,noinel},f} + I_{\text{in,noinel},b}}} \quad (28)$$

for the cases of with and without energy filters, respectively. The additional terms for phase contrast assume that the two beams which interfere have a $\pm 90^\circ$ phase relationship between their amplitudes, which is the case for defocus phase contrast optimized for a particular spatial frequency.

Example calculations of dose using these expressions, along with calculations for phase contrast in X-ray microscopy, are shown in Fig. 3. For imaging 2 nm thick protein features in 60 nm ice at 100 keV using defocus phase contrast, these calculations predict an electron exposure requirement of $1200 e^-/\text{nm}^2$, in reasonable agreement with experimental values of 600–700 e^-/nm^2 [9, 21].

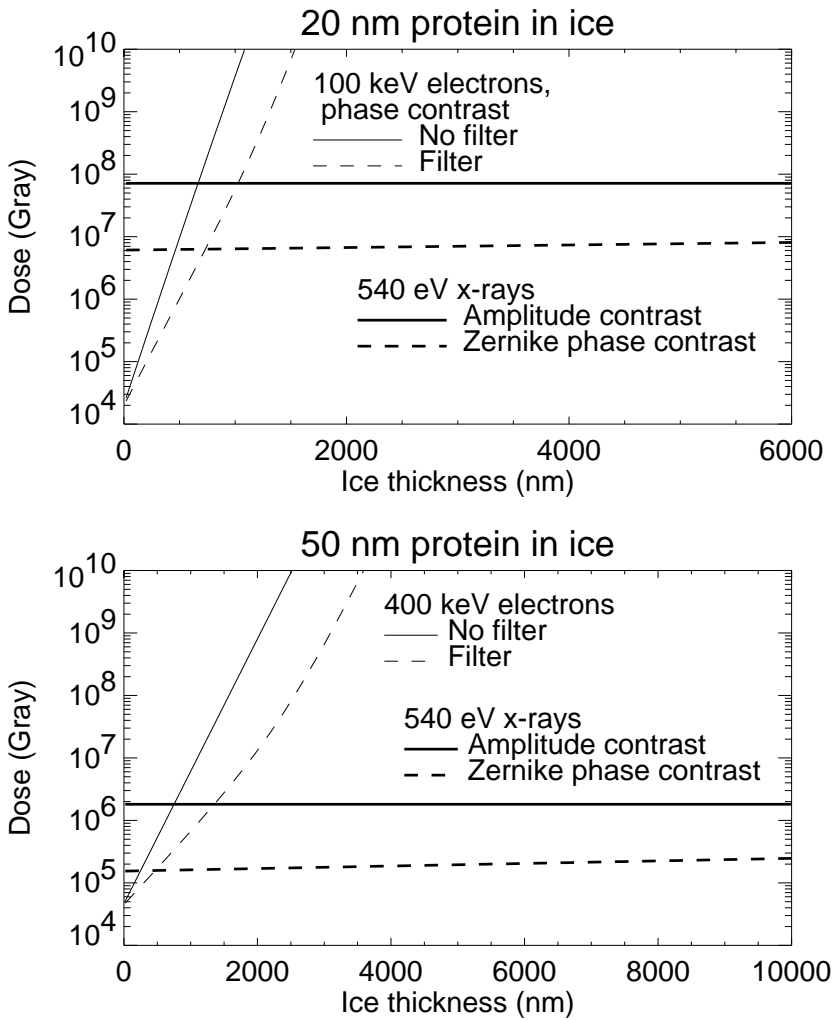


Fig. 3. Dose calculated for imaging protein features embedded in ice as a function of ice thickness. Note that these calculations assume that the feature is embedded exactly in the middle of the ice layer; furthermore, in the case of X-ray microscopy no allowance has been made for loss of high resolution signal due to microscope modulation transfer function. For the thinnest specimens (e.g., virus structures and macromolecular assemblies), electron microscopy provides higher resolution at low dose. For whole-cell-sized specimens, X-ray microscopy offers the ability to penetrate thick ice layers.

4 A Perspective on Electron and X-Ray Microscopy

We have presented here an outline of a calculation of image contrast and dose for electron microscopy of frozen hydrated specimens, and have compared the results both with experimental observations and with calculations for X-ray microscopy contrast and dose. These calculations suggest a dividing line between electron and X-ray microscopy:

- For specimens in ice layers of less than about 500 nm thickness, electron microscopy offers higher resolution at reduced radiation dose. One might then predict that, independent of improvements in X-ray microscope resolution, electron microscopy will remain the method of choice for studying macromolecular assemblies and virus structures in suspension in thin ice layers.
- For thicker ice layers (such as one might expect with whole cells which have been frozen hydrated), X-ray microscopes offer a great deal of freedom to handle exceptionally thick ice layers. It should be noted that the ratio of photoelectric absorption to coherent scattering for soft x rays is $\sim 10^4$, so that one would expect freedom from the blurring effects of multiple scattering in X-ray microscopy relative to electron or visible light probes. Note that while one can cryosection whole cells, up until now *serial* cryosectioning has not been possible so the only way to study three-dimensional structures in whole cells is through tomography.

One should also note that X-ray probes also offer intrinsic advantages for chemical state mapping [6]:

- In electron energy loss spectroscopy (EELS), the near-edge structure lies on top of a large background due to plural inelastic scattering, whereas inelastic scattering is negligible in the soft X-ray range.
- X-ray monochromators with an energy resolution of 0.05–0.10 eV are readily available, whereas EELS experiments tend to have an energy resolution of about 0.5 eV.

Of course, selective stains and labels are of great use in electron microscopy, and one can expect greater utility from further development of luminescence [23, 24] and gold sphere/dark field [25] labeling methods in X-ray microscopy as well.

Finally, it is worthwhile contemplating the ultimate limits of resolution in X-ray microscopy of frozen hydrated biological specimens. In electron microscopy, frozen hydrated specimens will “bubble” at exposures of 10^3 – 10^4 e^-/nm^2 , or at doses of between 3×10^7 and 3×10^8 Gray. The bubbles are comprised of hydrogen gas [26], and one may therefore expect bubbling to depend on the *rate* of dose deposition if hydrogen gas can diffuse through vitreous ice. Indeed, preliminary reports of X-ray cryomicroscopy by Schneider *et al.* indicate no observable radiation damage at the 50 nm level to doses of about 10^{10} Gray [27] delivered over 2 hours. If bubbling is not a limit, will cryogenic specimens prove to be indestructable? The experience of electron microscopy suggests otherwise; for example, loss of ~ 10 nm resolution structural detail is observed to take place

[28] at exposures of only $30 e^-/\text{nm}^2$ or 10^6 Gray (see also e.g., [29, 30]). Cryo methods may stop secondary radiolytical reactions, but they are powerless to prevent initial bond breakage.

Acknowledgements

We wish to thank Bob Glaeser, Michael Isaacson, Janos Kirz, and Richard Leapman for helpful discussions. This work was carried out under support from the National Science Foundation (ECS division) under Presidential Faculty Fellow award RCD 92-53618 (CJ).

References

1. E. Betzig, J. K. Trautman, T. D. Harris, J. S. Weiner, and R. L. Kostelak. Breaking the diffraction barrier: optical microscopy on a nanometric scale. *Science*, 251:1468–1470, 1991.
2. W. A. Carrington, R. M. Lynch, E. D. W. Moore, G. Isenberg, K. E. Fogarty, and F. S. Fay. Superresolution three-dimensional images of fluorescence in cells with minimal light exposure. *Science*, 268:1483–1487, 1995.
3. J. R. Breedlove, Jr. and G. T. Trammel. Molecular microscopy: fundamental limitations. *Science*, 170:1310–1313, 1970.
4. R. Henderson. The potential and limitations of neutrons, electrons and X-rays for atomic resolution microscopy of unstained biological molecules. *Quarterly Reviews of Biophysics*, 28(2):171–193, 1995.
5. D. Sayre, J. Kirz, R. Feder, D. M. Kim, and E. Spiller. Transmission microscopy of unmodified biological materials: Comparative radiation dosages with electrons and ultrasoft x-ray photons. *Ultramicroscopy*, 2:337–341, 1977.
6. M. Isaacson and M. Utlat. A comparison of electron and photon beams for determining micro-chemical environment. *Optik*, 50:213–234, 1978.
7. P. Götz. Calculations on radiation dosages of biological materials in phase contrast and amplitude contrast x-ray microscopy. In A. G. Michette, G. R. Morrison, and C. J. Buckley, editors, *X-ray Microscopy III*, volume 67 of *Springer Series in Optical Sciences*, pages 313–315, Berlin, 1992. Springer-Verlag.
8. R. R. Schröder. Zero-loss energy-filtered imaging of frozen-hydrated proteins: model calculations and implications for future developments. *Journal of Microscopy*, 166:389–400, 1992.
9. J. P. Langmore and M. F. Smith. Quantitative energy-filtered electron microscopy of biological molecules in ice. *Ultramicroscopy*, 46:349–373, 1992.
10. J. P. Langmore, J. Wall, and M.S. Isaacson. The collection of scattered electrons in dark field electron microscopy: I. elastic scattering. *Optik*, 38:335–350, 1973.
11. J. Wall, M. Isaacson, and J.P. Langmore. The collection of scattered electrons in dark field electron microscopy: II. inelastic scattering. *Optik*, 39:359–374, 1974. of Emin should be 2.
12. R. A. London, M. D. Rosen, and J. E. Trebes. Wavelength choice for soft x-ray laser holography of biological samples. *Applied Optics*, 28:3397–3404, 1989.
13. C. Dinges, A. Berger, and H. Rose. Simulation of TEM images considering phonon and electronic excitations. *Ultramicroscopy*, 60:49–70, 1995.

14. S. Q. Sun, S. L. Shi, and R. D. Leapman. Water distribution of hydrated biological specimens by valence electron energy loss spectroscopy. *Ultramicroscopy*, 50:127–139, 1993.
15. R. Grimm, D. Typke, M. Bärmann, and W. Baumeister. Determination of the inelastic mean free path in ice by examination of tilted vesicles and automated most probable loss imaging. *Ultramicroscopy*, 63:169–179, 1996.
16. M. Isaacson. Inelastic scattering and beam damage of biological molecules. In B. M. Siegel and D. R. Beaman, editors, *Physical aspects of electron microscopy and microbeam analysis*, pages 247–258, New York, 1975. Wiley.
17. M. J. Berger and S. M. Seltzer. Tables of energy-losses and ranges of electrons and positrons. Technical Report Publication 1133, Committee on Nuclear Science, National Research Council, National Academy of Sciences, Washington, D.C., 1964. Chapter 10, pp. 205–268, Library of Congress catalogue number 64-60027.
18. M. Isaacson, 1994. Personal communication.
19. L. Reimer. *Transmission electron microscopy: physics of image formation and microanalysis*. Springer-Verlag, Berlin, third edition, 1993. Springer Series in Optical Sciences **36**.
20. A. V. Crewe and T. Groves. Thick specimens in the CEM and STEM. I: Contrast. *Journal of Applied Physics*, 45:3662–3672, 1974.
21. R. R. Schröder, W. Hofmann, and J.-F. Ménéret. Zero-loss energy filtering as improved imaging mode in cryoelectronmicroscopy of frozen-hydrated specimens. *Journal of Structural Biology*, 105:28–34, 1990.
22. R. M. Glaeser. Limitations to significant information in biological electron microscopy as a result of radiation damage. *Journal of Ultrastructure Research*, 36:466–482, 1971.
23. C. Jacobsen, S. Lindaas, S. Williams, and X. Zhang. Scanning luminescence x-ray microscopy: imaging fluorescence dyes at suboptical resolution. *J. Microscopy*, 172:121–129, 1993.
24. M.M. Moronne, C. Larabell, P.R. Selvin, and A. Irtel von Brenndorff. Development of fluorescent probes for x-ray microscopy. In G. W. Bailey and A. J. Garratt-Reed, editors, *Proceedings of the 52nd Annual Meeting of the Microscopy Society of America*, pages 48–49, San Francisco, 1994. San Francisco Press.
25. H. N. Chapman, J. Fu, C. Jacobsen, and S. Williams. Dark-field x-ray microscopy of immunogold-labeled cells. *Journal of the Microscopy Society of America*, 2(2):53–62, 1996.
26. R. D. Leapman and S. Sun. Cryo-electron energy loss spectroscopy: observations on vitrified hydrated specimens and radiation damage. *Ultramicroscopy*, 59:71–79, 1995.
27. G. Schneider, B. Niemann, P. Guttman, D. Rudolph, and G. Schmahl. Cryo x-ray microscopy. *Synchrotron Radiation News*, 8(3):19–28, 1995.
28. J. F. Conway, B. L. Trus, F. P. Booy, W. W. Newcomb, J. C. Brown, and A. C. Steven. The effects of radiation damage on the structure of frozen hydrated HSV-1 capsids. *Journal of Structural Biology*, 111:222–233, 1993.
29. M. K. Lamvik. Radiation damage in dry and frozen hydrated organic material. *Journal of Microscopy*, 161:171–181, 1991.
30. M. F. Schmid, J. Jakana, P. Matsudaira, and W. Chu. Effects of radiation damage with 400-kV electrons on frozen, hydrated actin bundles. *Journal of Structural Biology*, 108:62–68, 1992.